JOURNAL OF GEOPHYSICAL RESEARCH, VOL. 105, NO. B10, PAGES 23,651-23,661, OCTOBER 10, 2000

Fracture process zone in granite

Arno Zang and F. Christian Wagner

GeoForschungsZentrum, Potsdam, Germany

Sergei Stanchits

U. S. Geological Survey, Menlo Park, California

Christoph Janssen and Georg Dresen

GeoForschungsZentrum, Potsdam, Germany

Abstract. In uniaxial compression tests performed on Aue granite cores (diameter 50 mm, length 100 mm), a steel loading plate was used to induce the formation of a discrete shear fracture. A zone of distributed microcracks surrounds the tip of the propagating fracture. This process zone is imaged by locating acoustic emission events using 12 piezoceramic sensors attached to the samples. Propagation velocity of the process zone is varied by using the rate of acoustic emissions to control the applied axial force. The resulting velocities range from 2 mm/s in displacement-controlled tests to 2 μm/s in tests controlled by acoustic emission rate. Wave velocities and amplitudes are monitored during fault formation. *P* waves transmitted through the approaching process zone show a drop in amplitude of 26 dB, and ultrasonic velocities are reduced by 10%. The width of the process zone is ~9 times the grain diameter inferred from acoustic data but is only 2 times the grain size from optical crack inspection. The process zone of fast propagating fractures is wider than for slow ones. The density of microcracks and acoustic emissions increases approaching the main fracture. Shear displacement scales linearly with fracture length. Fault plane solutions from acoustic events show similar orientation of nodal planes on both sides of the shear fracture. The ratio of the process zone width to the fault length in Aue granite ranges from 0.01 to 0.1 inferred from crack data and acoustic emissions, respectively. The fracture surface energy is estimated from microstructure analysis to be ~2 J. A lower bound estimate for the energy dissipated by acoustic events is 0.1 J.

1. Introduction

During rock fracture, stored elastic energy is released as heat, radiated elastic waves, and in the formation of structural defects like cracks, twins and dislocations. In particular, *Hoagland et al.* [1973] postulated that microcracking occurs in the vicinity of a macrocrack tip generating a "process zone." The geometry of the process zone of a tensile crack is first calculated by *Evans et al.* [1977] applying a critical stress microcracking criterion to the crack tip stress field equations. For shear cracks, *Rice* [1980] defined a zone of strength degradation at the crack tip (slip-weakening instability model) and developed a method to calculate the fracture energy from the work done in shear during the stress breakdown. On the basis of Rice's model, *Wong* [1982] estimated the shear fracture energy value of Westerly granite (10^4 J m^{-2}), which is ~2 orders of magnitude higher than the corresponding value of tensile cracks. Slip-weakening models are regarded as an extension to shear faults of "cohesive zone" (see next paragraph) models for tensile cracks [*Rice*, 1980; *Cowie and Scholz,* 1992a, 1992b]. The fracture process zone (FPZ) in rocks is defined as the region affected by microcracking and frictional slip surrounding the visible crack tip propagating under stress [*Labuz et al.*, 1983; *Swanson*, 1987; *Vermilye and Scholz,* 1998]. In contrast, the term damage zone is used to describe the accumulated deformation surrounding the fault as a whole [*Chester and Logan*, 1986].

Process zone models based on nonlinear fracture mechanics may be separated into cohesive [*Dugdale*, 1960; *Barenblatt,* 1962; *Labuz et al.*, 1987; *Cowie and Scholz*, 1992b; *Labuz and Biolzi*, 1998], postpeak behavior [*Goodier*, 1968; *Nemat-Nasser and Horii,* 1987], bridging [*Hoagland and Embury*, 1979; *Rossmanith*, 1983; *Hutchinson*, 1987; *Cox and Marshall,* 1994; *Shum*, 1996] and nonsingular stress models [*Wieghardt*, 1907; *Neuber*, 1937; *Hoshide*, 1993; *Dyskin*, 1997]. To extrapolate laboratory results to the field, it is a prerequisite to understand the micromechanics of the breakdown process at the fracture tip.

In laboratory experiments the FPZ was investigated in situ using advanced acoustic emission techniques [e.g., *Lockner,* 1996; *Lei et al.*, 2000] and ultrasonic probing [e.g., *Granryd et al.,* 1983; *Swanson*, 1987]. *Moore and Lockner* [1995] studied the crack microstructure surrounding an experimentally induced shear fracture. In the process zone, tensile microcracks are oriented 30° to the fracture on average. Crack density of tensile microcracks increases substantially near the fracture. The width of the FPZ in rock is considered a material property, and it was found to increase with increasing grain size [*Ouchterlony,* 1980; *Zietlow and Labuz*, 1998]. *Barton* [1982] observed a range in width from ~5 to 10 times the average grain diameter. In comparison, residual elastic strains in quartz grains of

Paper number 2000JB900239.
0148-0227/00/2000JB900239$09.00

Tennessee sandstone relax within a 5 mm wide region on either side of a tensile fracture [*Friedman et al.,* 1972].

Field observations on natural faults indicate that crack density of the FPZ decreases as the logarithm of the distance to the fault [*Vermilye and Scholz,* 1998]. Microfracture density was observed to reach a maximum value independent of fault length. Vermilye and Scholz found that the logarithm of FPZ width increases linearly with the logarithm of the fault length. *Cowie and Scholz* [1992a] suggested that fault growth related to earthquake rupture is small and may not exceed ~1% of the initial fault length. For larger earthquakes the magnitude was suggested to scale with size of the nucleation zone [*Ellsworth and Beroza*, 1995].

In this paper we investigate the process zone of experimentally induced shear fractures in Aue granite. Propagation of the fracture through the granite is observed in situ by locating acoustic emission hypocenters at different growth rates. Study of the acoustic emissions is compared to the crack microstructure after deformation.

2. Experimental Technique

We performed nine uniaxial compression tests on Aue granite designed to induce a predefined shear rupture in the sample. To initiate a high stress concentration, a steel plate that covered 80% of the top surface was placed between specimen and piston (see Figure 1a). Diameter of the cylindrical samples was 50 mm, and their length was 100 mm. The unorthodox (asymmetric) loading technique including stress calculations at the onset of fracture is evaluated and compared to standard symmetric rock testing in an earlier study [*Zang et al.*, 1998]. From this work, failure is expected to initiate in tensile mode at the edge of the loading plate and to propagate with a dominating shear component into the unloaded part of the asymmetrically loaded cylinder. Both normal displacement (tensile) and finite shear displacement are observed in deformed cores. The advantage of the asymmetric test compared to standard symmetric tests is to know in advance the nucleation patch and the propagation path of the fracture.

Two different types of Aue granite (Table 1, Agw and Agr) were tested. The major minerals in red Aue granite (Agr) are 30 vol % quartz, 40 vol % plagioclase, 20 vol % potassium feldspar, and 10 vol % mica. The average grain size is 1.3 mm, and porosity is 1.3%. White Aue granite consists of 30 vol % quartz, 35 vol % plagioclase, 25 vol % potassium feldspar, and 5 vol % mica. The average grain size is 1.7 mm, and porosity is 0.3%.

To monitor acoustic emissions (AE) emitted during fracture propagation, 12 piezoceramic transducers were attached to the specimen (Figure 1b). The AE data aquisition system is identical to the one that was used in our earlier studies [*Zang et al.,* 1998]. The AE data were used to determine location, magnitude, and type of the acoustic signals generated during fracturing. Three tests are operated with a displacement-controlled rate of 0.3 μm/s. For all other experiments we used the AE rate recorded at sensor 5, 10, or 12 (Table 1) as feedback signal to servocontrol axial force and stabilize stress drop [*Lockner et al.*, 1991]. The trigger level of the rate control sensor was varied (Table 1), first, to produce fractures of different length ranging from 0 mm (Table 1, Ag22w) to 93 mm (Table 1, Ag53r) and, second, to produce faults with different propagation velocities (no trigger = displacement controlled ≈ 2 mm/s (fast fault), 60 mV trigger level ≈ 2 μm/s (slow fault)).

At fixed intervals during an experiment a 400 volt ultrasonic pulse was emitted from sensor 12 across the future trace of the fracture in the sample (Figure 1a). The amplitude and velocity data of the generated *P* wave pulses were analyzed as a function of time or increasing fault length, respectively.

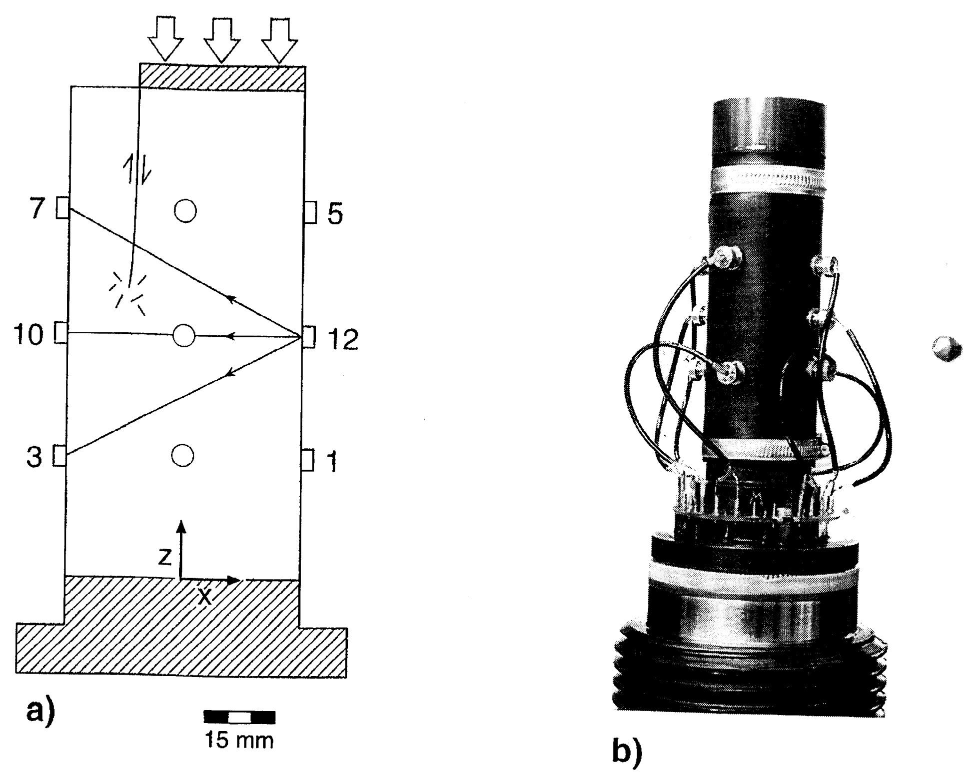

Figure 1. (a) Schematic diagram and (b) photograph of sensor and loading geometry in an asymmetric (confined) compression test.

Table 1. Mechanical, Acoustic, and Crack Inspection Data Collected From Uniaxial Compression Tests With AE Rate Control on Aue Granite Cores (Ag)

	Experiment, Core								
	970814, Ag18r	970815, Ag21w	970924, Ag22w	970925, Ag23w	980505, Ag19r	980701, Ag51r	980721, Ag53r	980730, Ag54r	980805, Ag55r
Mechanical Data									
Critical force K_c, kN	149	137	119	88	157	137	95	150	150
Critical strain ε_c, ‰	2.0	1.4	1.6	1.9	2.6	2.2	1.5	2.2	2.3
Critical time t_c, s	933	491	755	718	1255	1473	1000	1000	1300
Duration time t, s	1640	3960	757	732	2529	15600	41218	30000	50000
P wave velocity v_p, km/s	3.9	4.9	5.0	5.0	4.0	4.3	4.3	4.3	4.1
Acoustic Emission									
Location and trigger sensor	12, 1 - 8	12, 1 - 8	12, 1 - 8	12, 1 - 8	12, 1 - 8	12, 1 - 8	12, 1 - 8	12, 1 - 8	12, 1 - 8
Trigger level, mV	152	300	300	300	152	300	300	280	300
Rate control sensor	12	12	12	12	10	5	5	5	5
Trigger level, mV	600	300	300	300	300	60	60	60	60
Detected events, N	6000	6000	210 stop	400 stop	5000	2000	8000	6000	9000
N_{Loc}: R (µs), Simplex	1928	2266	66, R<2	155, R<2	1468, R<2	1229, R<2	3596, R<2	1761, R<2	4955, R<2
N_{Loc}: R (µs), Gauss	1204, R<1	1321, R<1	175	218	830, R<2	1184, R<2	1978, R<2	490, R<2	3972, R<2
AE for polarity statistics	999	165	196	69		632 550	423 411		
T type, %	18	21	19	16		18 21	23 15		
S type, %	68	67	64	70		76 74	67 75		
C type, %	14	12	17	14		6 5	10 10		
Broadband sensor events	4044	6302	-	-	12664	334	1893	2439	-
Trigger level, mV	500	500	-	-	250	500	500	500	-
Energy E, mV s	0.8	3	-	-	0.2	12	105	33	-
Pulse duration T, ms	5	17	-	-	9	1	5	4	-
Crack Inspection									
Thin section 30 x 100 mm	+	+	+	+	-	+	+	-	-
Fracture length L, mm	75	90	0	88	-	55	93	-	-
Number of cracks N_c	678	548	0	400	-	161	531	-	-
Crack density ρ_{max}, mm^{-1}	4.9	5.4	0	-	-	2.6	7.8	-	-
Crack width a_{max}, µm	40	30	0	60	-	30	50	-	-

R Travel time residual, + Thin section prepared.

After deformation the granite cores were vacuum impregnated with blue epoxy resin and cut in two halves. Optical thin sections were prepared with a size of 30 x 100 mm that contain the shear fracture. Only open (filled with blue epoxy), deformation-related cracks adjacent to the fracture trace are inspected. For one specimen the background crack density is determined (0.6±0.2 mm^{-1}). The minimum crack aperture and crack length that were resolved optically were 5 and 10 µm, respectively. Crack density, orientation distribution, and crack types were quantified perpendicular and parallel to the shear fracture trace [*Janssen et al.,* 2000].

The relevance of our experiments for understanding faulting in the Earth's crust comes from three facts. First, the physics of the process zone of a propagating rupture is poorly understood even in the end-member case of zero confinement. Second, in the shallow crust a combination of tensile and shear mode cracks may lead to fault rupturing. Third, the controlled variation of the propagation velocity of the fault allows us to bridge the gap between previously published laboratory acoustic emission results on dynamic fracture [*Lei et al.,* 2000] and quasi-static rate-controlled tests [*Lockner et al.,* 1991]. A second study with a series of confined asymmetric tests is under way which focuses on the process zone in different materials. For reference, two data points from the second study are included in the discussion (see section 4.1, Figure 12).

3. Experimental Results

In Table 1 mechanical, acoustic data and microstructure results are summarized for the three white and six red granite cores that were tested. The mechanical data include the critical force K_c, critical strain ε_c, and critical time t_c at the onset of the shear fracture as well as the duration time of the experiment t and the P wave velocity of stress-free material v_P. Acoustic emission data include the setup conditions for 12 location sensors and one AE rate control sensor. Also shown is the total number of acoustic emission events that were registered N and located N_{Loc}. For high-quality acoustic signals, first pulse motions are used to calculate event polarities. The polarity value (POL) is defined as the ratio of dilatational to compressional first pulse motions normalized by the number of location sensors. It ranges between -1 (T-type (tensile) event) and 1 (C-type (collapse) event). For S-type (shear) events the range $-0.25 \leq POL \leq 0.25$ is defined [*Zang et al.,* 1998]. Maximum values of equivalent AE energy (E^*) and AE duration times (T^*) that were registered with a broadband sensor (Figure 1a, sensor 9) are listed for comparison. Optical microscopy results include the final length of the shear fracture L and the total number of process zone-related microcracks (number N_c, maximum crack density ρ_{max}, and maximum crack aperture a_{max}).

3.1. Acoustic Emission Data

To locate AE hypocenters, we used a least squares iterative technique to minimize travel time residuals (Table 1, Gauss) and compared the results to those obtained with a different location procedure (Downhill Simplex [*Press et al.,* 1987]). The located acoustic emission events associated with fracture propagation in sample Ag53r are shown in Figure 2. AE hypocenters are displayed in a horizontal (xy) and two vertical (xz, yz) projections of the cylindrical specimen for different time slices. AE events are determined with an absolute location error of 3 mm (Simplex, N_{Loc}, Table 1). From the xz (cross section) of Figures 2a-2d, four stages of the fracture growth are documented. A dense cloud of AE defines a zone of distributed

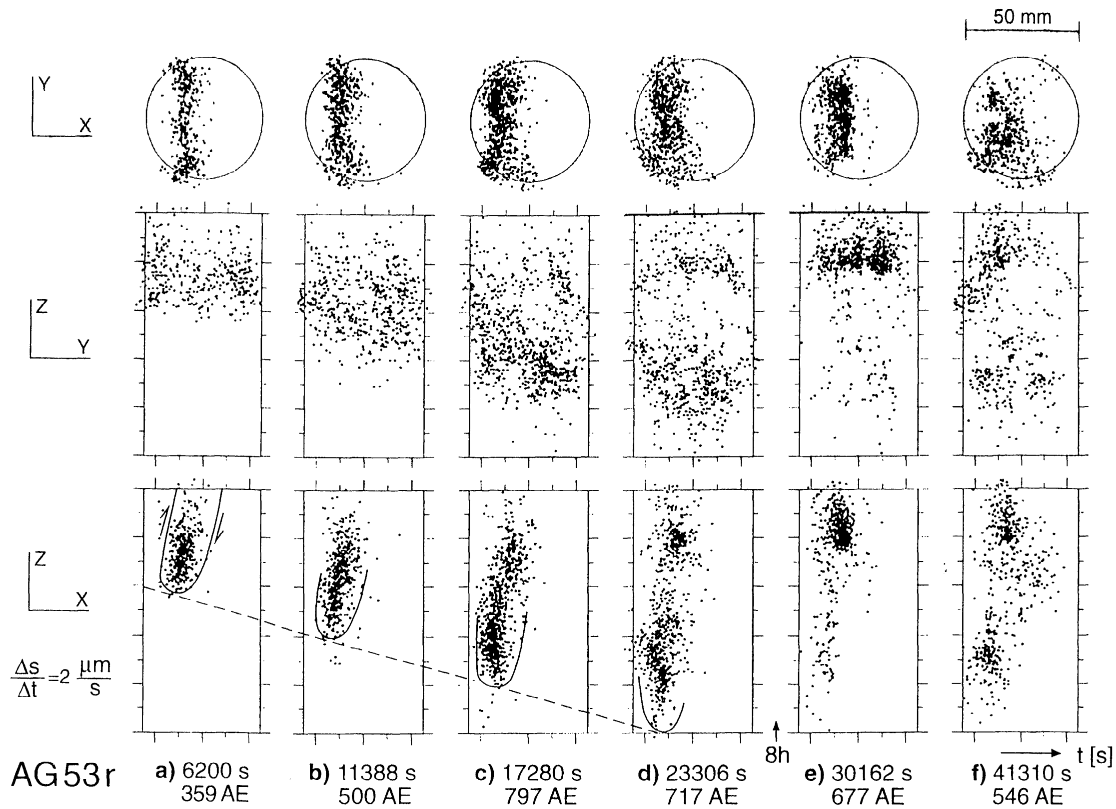

Figure 2. Hypocenter locations of 3596 acoustic emissions (dots) during the asymmetric test on Aue granite Ag53r in three orthogonal projections of the cylinder versus time of the experiment (total duration 11.5 hours).

acoustic activity indicated by the solid line that propagates from top to bottom through the sample. We consider this AE cloud to indicate the fracture process zone.

The bottom end of the AE cloud (Figures 2a-2d, *xz* projection, straight dashed line) was used to determine the velocity of the propagating FPZ; for specimen Ag53r this velocity was 2 μm/s. The width of the FPZ in *xz* projection is also indicated by the solid line in Figures 2a-2d. The two time slices displayed in Figure 2e and 2f show the nucleation of a second fracture at top of the granite core after the AE cloud of the first rupture has traversed the sample completely (Figure 2d). The second rupture is not further considered in this paper.

The average polarity values from six AE rate-controlled tests (Table 1, polarity statistics) show that on average 70% of AE are S-type events. They clearly dominate the fracture process in Aue granite compared to tensile (20%) and collapse sources (10%). This is in agreement with previous findings on the same material [*Zang et al.*, 1998]. For type S events with equal ratio of dilatational and compressional first motions, focal mechanisms are determined earlier by fitting measured first pulse amplitudes to an assumed double-couple radiation pattern. While hypocenters of large type S events align parallel to the later fracture plane, their single-fault plane solutions show no coherent orientations [*Zang et al.*, 1998]. A recent study by *Lei et al.* [2000] added 32 transducers to better constrain the single slip mechanism. On the basis of their sensor polarity ratio they could resolve four crack categories with complex slip mechanisms involving events with both tensile and shear components.

3.2. Ultrasonic Pulse Transmission

Results from ultrasonic pulse transmission during deformation of core Ag53r are shown in Figure 3. Ultrasonic waves emitted from transducer 12 and recorded at transducers 3, 7, and 10 cross the trace of the future fracture and are thus affected by microcracking in the process zone. The initial amplitude is A_0 = 400 mV at t=0, and the final amplitude at transducer 3 at time t= 23306 s is A = 20 mV. The drop in amplitude is $\alpha = 20 \log(A/A_0)$ = 26 dB (Figure 3). The drop in amplitude as recorded at different receivers is shifted, and from this a propagation velocity of the process zone of 4 μm/s is calculated. This value is in agreement with the velocity deduced from hypocenter data. In Figure 3b we plot the velocities of *P* waves. Velocity values in all channels first increase by ≈ 5% owing to crack closure as the core is initially compressed. Dilatant microcracking then leads to a velocity reduction of ≈ 10%. Figure 3c is a plot of the registered cumulative number of AE and the applied load versus duration time of the experiment. At time t=23306 s the tip of the acoustic process zone reached the bottom of core Ag53r (Figure 2d). The optically visible fracture tip in this experiment stopped 7 mm distance above the bottom end of the sample (Table 1, Ag53r, L=93 mm).

It has to be pointed out that the general trend in velocity and amplitude behavior during the propagation of the process zone is the same for unconfined and confined (up to 40 MPa) asymmetric tests, where significant normal stress will force the fracture closed.

3.3. Crack Microstructure

The length of the macroscopically visible shear fracture (Table 1, L) is determined from epoxy-saturated cores after they were cut in two halves (Figure 4a). The width of the macrofracture is larger at top of the core near the nucleation patch compared to the lower end, where it branches and stopped at 7 mm above the bottom end of the core. The fracture is

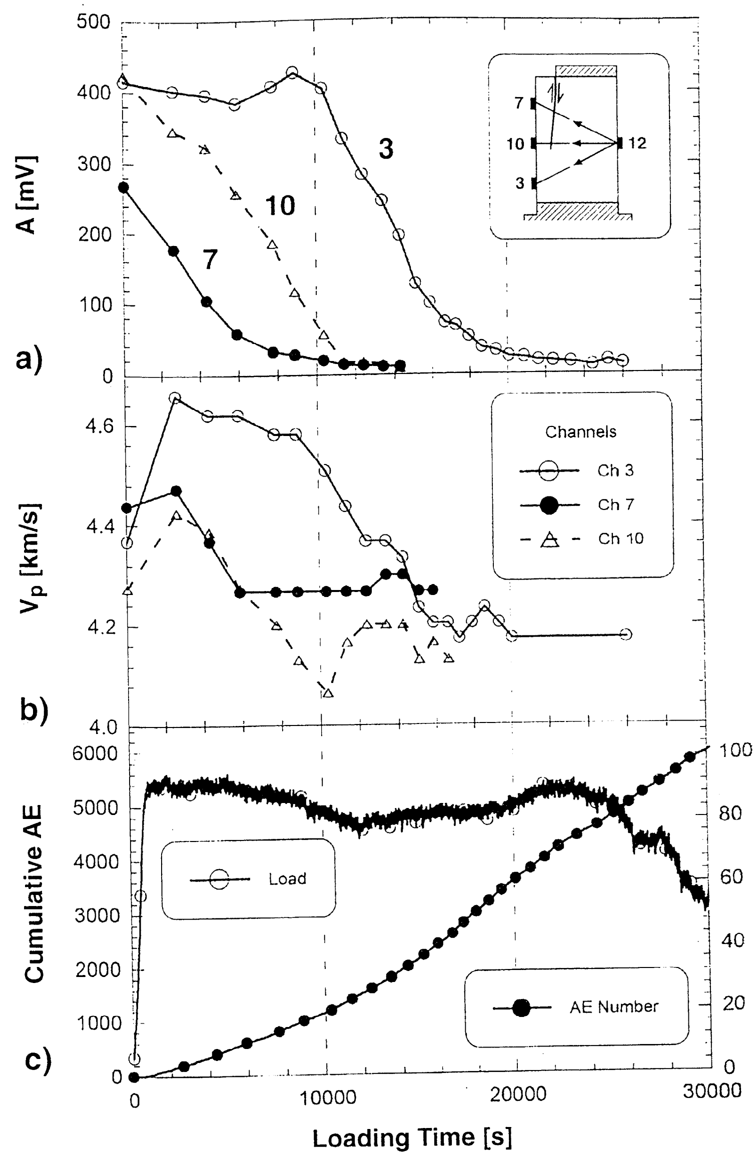

Figure 3. (a) Amplitude and (b) velocity of P wave from pulse transmission experiment versus time for core Ag53r. (c) Applied load and cumulative number of registered acoustic events, shown for reference.

oriented with 5° to the vertical axis of the core. In thin section (Figure 4b) the width of the macrofracture is ≈150 μm, and the widths of the associated microcracks are smaller by about an order of magnitude. In Figure 5a the width of the macrofracture is plotted versus the length for sample Ag23w. The maximum aperture is 300 μm at 65 mm from the top of the 88 mm long fracture. Note that in this experiment (Table 1, 970925) the piston was retreated by hand as soon as 400 AE signals were detected. In Figure 5b the total number of microcracks counted in sample Ag53r is plotted versus distance perpendicular to the shear fracture trace (x_s axis). Within 2.8 mm of the fracture trace the number of cracks increases between 5 and 10 times toward the centre of the fracture. Among the cracks with an aperture > 5 μm observed in the FPZ, intragranular cracks dominate the entire cross section (Figure 5b). Transgranular cracks are restricted to the central part ($x_s \leq$ 1.4 mm), and the proportion of intergranular cracks increases away from the center ($x_s \geq$ 2.8 mm). Detailed microstructural investigations will be published elsewhere [*Janssen et al.,* 2000]. Table 1 summarizes the total number of microcracks N_c, maximum crack density ρ_{max}, and maximum crack aperture a_{max} analyzed in six thin sections. Microcrack densities measured along and perpendicular to the main fracture are presented below in context with the acoustic emission hypocenter distribution in order to illustrate the geometry of the fracture process zone.

3.4. Geometry of the Process Zone

Figure 6 shows the cumulative AE hypocenters in xz projection (Figure 6, dots) for two granite specimens with different fracture lengths (Ag51r and Ag53r). Superimposed on the AE hypocenters are the traces of the shear fractures as observed in thin sections of the two specimens. In both samples the fracture trace (Figure 6, subvertical gray line) coincides with the maximum density of AE hypocenters. Note that the low density of located AE hypocenters within 20 mm from the top and bottom of the specimens is partly due to the geometry of the transducer array (Figure 1a). This likely explains why we observed only a few AE around the fracture tip in sample Ag53r

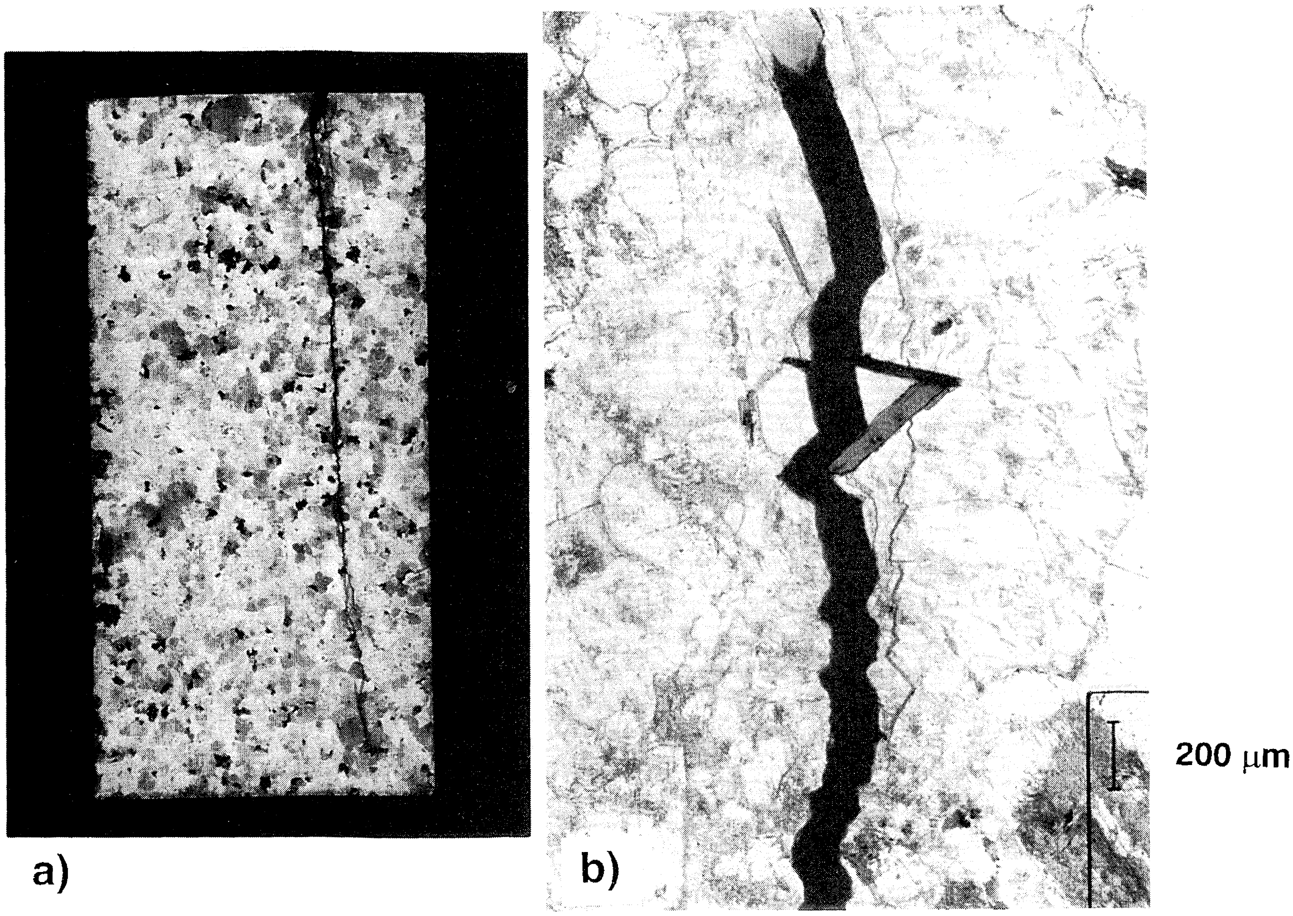

Figure 4. Trace of fracture (subvertical black line) in xz projection from asymmetric compression tests (a) inside an half core Ag53r saturated with epoxy resin and (b) within a thin section of core Ag23w .

(Figure 6b, L=93 mm, z=7 mm) as opposed to sample Ag51r in Figure 6a (L = 55 mm, z = 45 mm). Rectangles denoted SI to SV indicate the location of cross sections that were optically investigated in detail. Each rectangle consists of 4 (vertical) x 7 (horizontal) = 28 fotos covering an area of 1.4 x 0.9 mm in the xz plane of the cores. The maximum crack density observed in these sections is 2.6 mm^{-1} for Ag51r and 7.8 mm^{-1} for Ag53r (Table 1, ρ_{max}).

In Figure 7 the crack density and cumulative number of AE are shown perpendicular to the trace of the shear fault cutting through sample Ag53r. The crack density represents an average from profiles SI to SV. The total number of located AE is plotted versus the distance x_S to the macrofracture in Figure 7. The crack density and the number of AE decrease as the logarithm of the distance from the center of the shear fracture:

$$\rho\,(x_S) = -\,a \log\,(x_S) + b, \qquad (1)$$

where $\rho\,(x_S)$ denotes either crack density or cumulative AE number (Figure 7). The constants a and b in (1) were determined separately from semilogarithmic plots for the left ($x_S \leq 0$) and the right side of fracture ($x_S \geq 0$), with maximum density at x_S = 0, $\rho\,(x_S)$ normalized to 1. Note that the top surface of the sample was not loaded left of the fracture (Figure 1a). To the right of the fracture the sample was loaded by the top piston. Constants a and b of four granite samples are given in Table 2. The data are based on the analysis of 4950 AE and 1918 process zone-related cracks. The slope a averaged over four samples indicates that the AE density drops off asymmetrically on both sides of the fault (unloaded 0.96±0.13, loaded 0.53±0.11). Average crack density falls off symmetrically (0.67±0.06). Note that in Figure 7 only deformation-related cracks are considered to calculate the crack density. The background crack density value has to be added to obtain the total crack density.

The width of the process zone based on crack density and AE number distribution is determined from plots similar to Figure 7 for all samples from Table 2. First, the standard deviation of the crack and AE distribution as in Figure 7 was determined. The width of the process zone was then defined as twice the standard deviation (Figure 8a and Table 3). On the basis of the average value of four cores the width of the process zone defined by the AE distribution (w_{AE}=12±4 mm) is 4 times the width of the optically defined process zone (w_C= 3±1 mm). These values represent a lower bound for the width of the process zone. They are plotted versus fault length in Figure 8a.

In Figure 8b the total displacement along the shear fracture based on piston displacement projected on the fracture trace is plotted versus the length of the fracture. The Agr specimens indicate an approximate linear increase of shear fracture displacement u versus length L with $\Delta u/\Delta L \approx 0.3$ mm/ 100 mm, which was also suggested in fault growth models [*Cowie and Scholz*, 1992b]. The white granite specimen (Figure 8b, Ag21w) falls off this linear relationship and is characterized by a smaller total displacement compared to a red granite with the same fracture length.

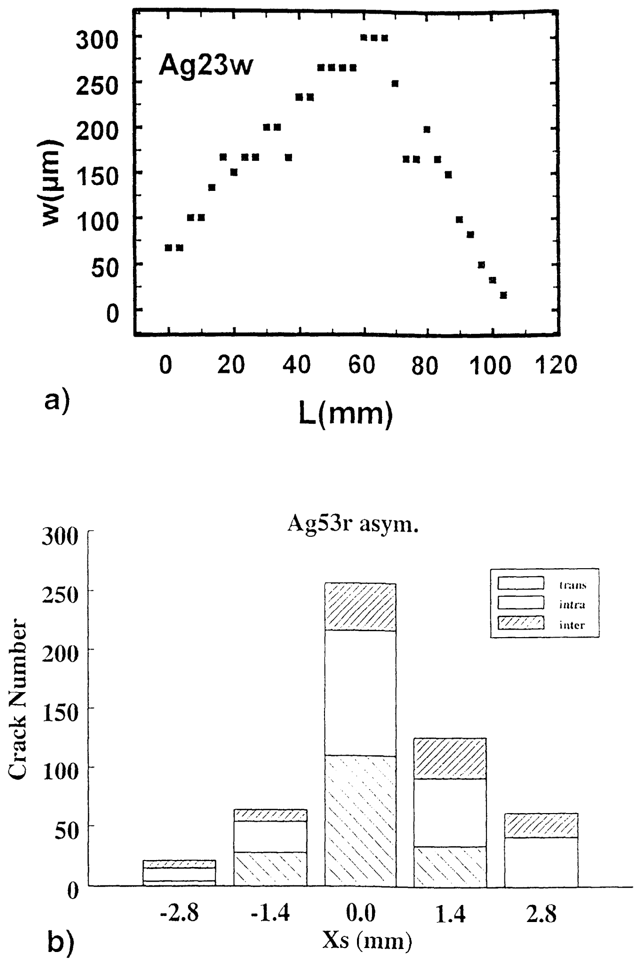

Figure 5. (a) Width of macrofracture versus length observed from thin section analysis of core Ag23w. (b) Histogram of process zone-related crack types perpendicular to the fracture.

3.5. Event Amplitudes and Fault Plane Solutions

In Figure 9 the average AE amplitudes of specimens Ag51r and Ag53r are plotted versus x_s axis perpendicular to the fracture trace. First, the maximum amplitude of a single event as received on 12 channels is averaged. Subsequently, this value is used to form a sliding average in 2 mm steps along the x_s axis for all hypocenters. In general, the amplitude of acoustic events increases as the center of the shear fracture is approached, irrespective of fracture length (Ag51r: L=55 mm; Ag53r: L=93 mm). As was observed for AE numbers (Figure 7), the event amplitudes (Figure 9) decrease asymmetrically on both sides of the fault.

In Figure 10 average fault plane solutions are determined for all S-type events of sample Ag53r for time $t \leq 23306$ s. For this purpose, all S-type events (Figure 10a, N_{Loc}= 1689) are separated into events occurring on the dilatational side of fault (Figure 10b, N_{Loc}= 767) and events occurring on the compressional side of fault (Figure 10c, N_{Loc}= 922). Average fault plane solutions are presented in lower (Figure 10, top) and side focal hemisphere projection (Figure 10, bottom). The former presentation is a standard in seismology, and the latter is chosen to have an independent measure of the fault dip based on the radiation pattern of acoustic emissions. White color in the Schmidt net projection denotes 50% dilatational, and black color denotes 50% compressional first pulse motions determined from 12 AE seismograms averaged over the total number of events under consideration. The dashed line in all projections indicates the zero-percentage isoline. No significant differences are found between signals generated on the dilatational and compressional side of the fault.

4. Discussion and Conclusions

4.1. AE and Crack Distribution in the Process Zone

Figure 11 is a synoptic cartoon of the process zone surrounding the shear fractures in Aue granite. On the basis of the distribution of acoustic emissions (w_{AE}) the width of the process zone perpendicular to the fracture trace (Figures 7 and 8a) is between 4 and 5 times larger than that based on the distribution of optically visible cracks (w_c) (Table 3). For red Aue granite this corresponds to a 9 grain diameters wide "acoustic" FPZ as opposed to a 2 grain diameters wide "optical" FPZ. Both values are somewhat arbitrary and present lower limits since they depend on the AE trigger level, the magnification reached in the optical microscope, or simply the definition used for the width of the FPZ. It is likely that with better resolution of the microstructure, w_c will approach w_{AE}. However, AE may also be emitted by twinning or dislocation motion and may not always be caused by the formation of a microcrack. On average, ~2% of cracks observed in the microscope produce detectable acoustic emissions. We calculate this number by combining the average area of the visible process zone (36×10^{-4} m^2), the average width of the acoustic process zone (w_{AE} = 12 mm), and the measured crack density value

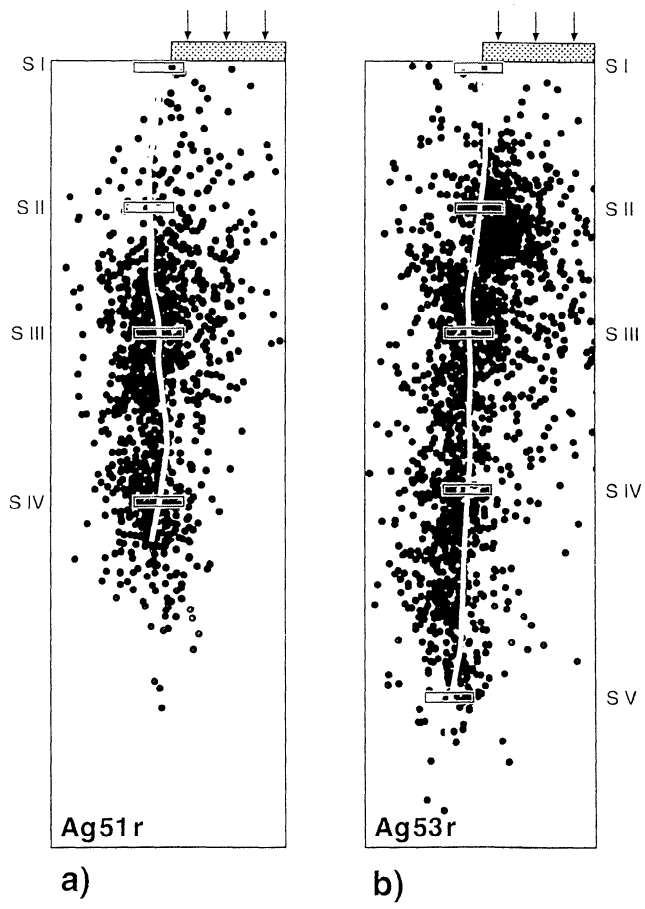

Figure 6. Cumulative acoustic emission hypocenters (dots) compared to the observed fracture trace (gray subvertical line) for two red granite cores. In Figure 6a the length of the fracture is 55 mm, and in Figure 6b it is 93 mm.

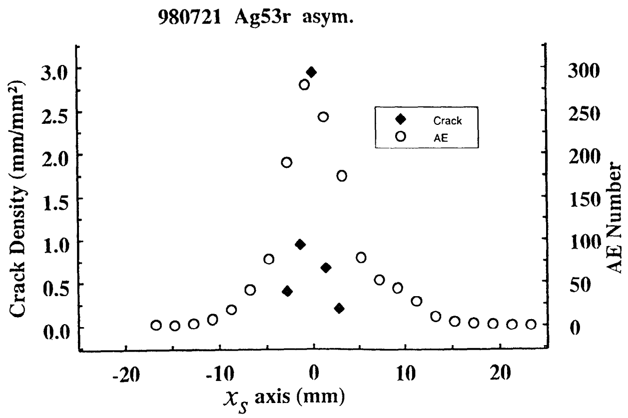

Figure 7. Density of process zone-related microcracks (left ordinate) observed in the microscope and the number of acoustic emissions (right ordinate) perpendicular to the trace of fracture (x_S axis) inside core Ag53r.

(c_{max} = 5 mm^{-1}). Therefore 2.7x10^5 cracks correspond to 6000 AE detected in the process zone.

We also found that ~70% of the AE events are S type, i.e., their source is likely a shear event. Our result of dominating type S cracking events in unconfined asymmetric granite tests is in agreement with *Lei et al.*'s [2000] findings on triaxially tested hornblende schist where the damage zone is characterized by major shear cracking from polarity statistics measured on 32 sensors. However, even in high-resolution scanning electron microscopy, these shear cracks may not be detected [*Wong*, 1982]. This is supported by microstructural investigation of sample Ag22w, where 210 AE were detected, but no cracks could be unambiguously related to the experimentally induced deformation (Table 1).

Lockner et al. [1991] performed deformation experiments on Westerly granite at 50 MPa confining pressure and studied nucleation and growth of a shear fracture. On the basis of located AE events they report a width for the FPZ of 1-5 mm. *Moore and Lockner* [1995] investigated the FPZ around a shear fracture produced experimentally in Lockner et al.'s Westerly granite sample G2 with an average grain size of 0.75 mm. With the definition used in this study the FPZ is ≈ 10 mm wide, i.e., ≈ 13 times the average grain size. For tensile fractures, *Zietlow and Labuz* [1998] observed that the process zone width increases with the logarithm of the grain size.

The AE distribution on both sides of the shear fracture is asymmetric with a steeper decrease in AE on the dilatational side (Table 2, $a \approx -1.0$) than on the compressional side (Table 2, $a \approx -0.5$). The average amplitude distribution of AE across the fracture is also asymmetric with a steeper decrease in amplitude toward the dilational side (Figure 9). This is in agreement with results from three-dimensional finite element modeling of the

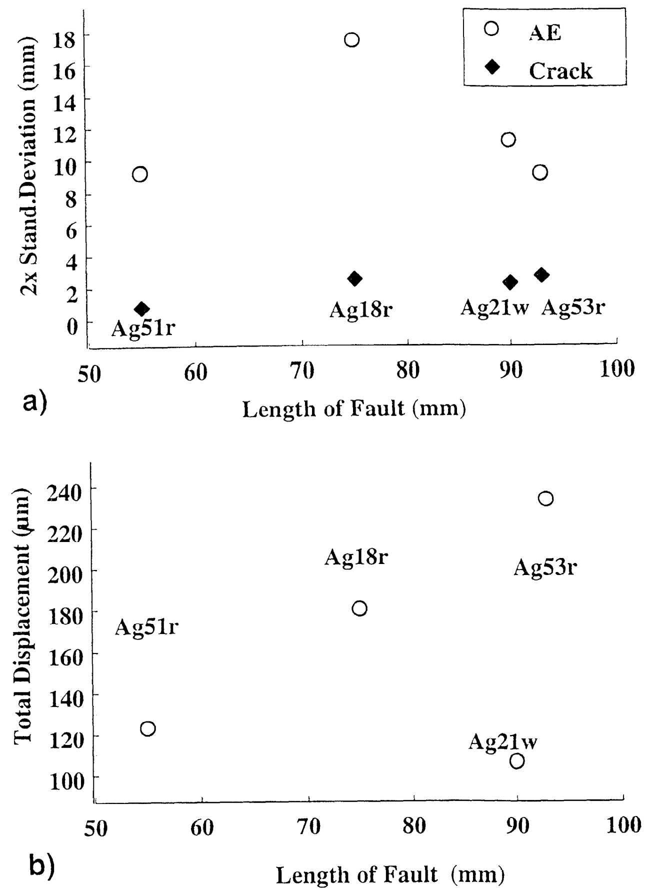

Figure 8. Width of fracture process zone (a) defined as twice the standard deviation from average values in AE and crack density distribution profiles perpendicular to fault and (b) total displacement of shear fracture, plotted versus fault length.

stress distribution in the sample at the onset of fracture [*Zang et al.*, 1998]. The stress distribution is asymmetric and shows a steep drop toward the free surface of the core, i.e., the dilational side of the future fracture. However, an attenuation in the process zone may effect distribution of AE densities and amplitudes. *Moore and Lockner* [1995] suggested a symmetric decrease in crack density on both sides of a shear fracture. Moore and Lockner found that the microcrack density on the dilational side of the propagating fracture was consistently higher than on the compressional side, as predicted in the model of *Reches and Lockner* [1994] and observed in a field study by *Vermilye* [1996]. We observed the opposite, i.e., that crack densities are mostly higher on the compressional side of the shear fracture. Also, the AE distribution indicates a larger

Table 2. Results of Calculated Constants (Equation (1), a and b) From Semilogarithmic Plots of AE Number and Crack Density Versus x_S Axis Given Separately For the Unloaded (Dilatational) and Loaded (Compressional) Side of Fractures in Four Granite Cores

Core	Unloaded[a]		Loaded[a]		Unloaded[b]		Loaded[b]	
	$\|a\|$	b	$\|a\|$	b	$\|a\|$	b	$\|a\|$	b
Ag18r	1.09	1.41	0.41	0.61	0.68	0.34	0.58	0.47
Ag21w	1.04	1.37	0.58	0.72	0.64	0.37	0.67	0.38
Ag51r	0.89	0.98	0.46	0.58	0.74	0.27	0.76	0.24
Ag53r	0.80	0.89	0.66	0.86	0.62	0.41	0.67	0.35

[a] Data based on the analysis of 4950 AE.
[b] Data based on the analysis of 1918 cracks.

Table 3. Geometry of the Process Zone and Fault Scaling Relationships[a]

Core	Fault Zone[b]		Width of Process Zone[c]		$d/2L$	$w_{AE}/2L$	$w_c/2L$	w_{AE}/d	w_c/d
	d, μm	$2L$, mm	w_{AE}, mm	w_c, mm	(x 0.001)				
Displacement-Controlled Tests									
Ag1r	211	170	14.8	-	1.2	0.09	-	70	-
Ag15w	161	180	19.9	-	0.9	0.11	-	124	-
Ag16w	271	202	20.4	-	1.4	0.10	-	75	-
AE Rate-Controlled Tests									
Ag18r	180	150	17.3	3.1	1.2	0.12	0.02	96	17
Ag21w	106	180	11.1	3.4	0.6	0.06	0.02	101	33
Ag23w	151	176	-	-	0.8	-	-	-	-
Ag51r	123	110	9.2	1.3	1.0	0.08	0.01	74	10
Ag53r	233	186	9.0	4.3	1.2	0.05	0.02	38	18

[a] The range of $d/2L$ observed in nature is 0.01, the theoretical range of $w/2L$ and w/d is 0.01-0.1 and 1-10, respectively [after *Scholz et al.* 1993].

[b] For fault zone, d is fault shear displacement, and $2L$ is total fault length.

[c] For process zone, w_{AE} is acoustical, and w_c is optical width (double standard deviation).

number of AEs and, on average, higher amplitudes on the compressional side. We suspect that the discrepancies are related to different boundary conditions of our experiments with those of *Lockner et al.* [1991]. This suggests that also in nature stress concentrators in a fault zone may largely influence crack density patterns. The situation can be different when crack densities of asymmetric confined tests become available.

While crack densities are important, failure criteria assume some critical total crack damage. One model [*Madden*, 1983; *Lockner et al.*, 1992; *Lockner*, 1993] suggests that the important parameter is the ratio of crack spacing to crack length for the population of cracks that first interact. We measured crack spacings and crack length distributions in Aue granite only for one specimen [*Janssen et al.*, 2000]. In this case (Ag21w) the crack density drops from 5.37 mm^{-1} in the center of the fault (x_S= 0) to 1.43 mm^{-1} away from the fault trace (x_S= 5.6 mm). The average crack spacing value increases from (70±50) μm at x_S= 0 to (200 ±79) μm at x_S= 5.6 mm. While the crack density drops by a factor of 3.8 with distance from fault, the spacing increases by a factor of 2.9 for corresponding distances. Further work is needed to comment on failure implications.

Scholz et al. [1993] and *Reches and Lockner* [1994], in their models based on considerations of the crack tip stress field of a propagating fault, suggested that tension cracks on the compressional side should be oriented with a smaller angle to

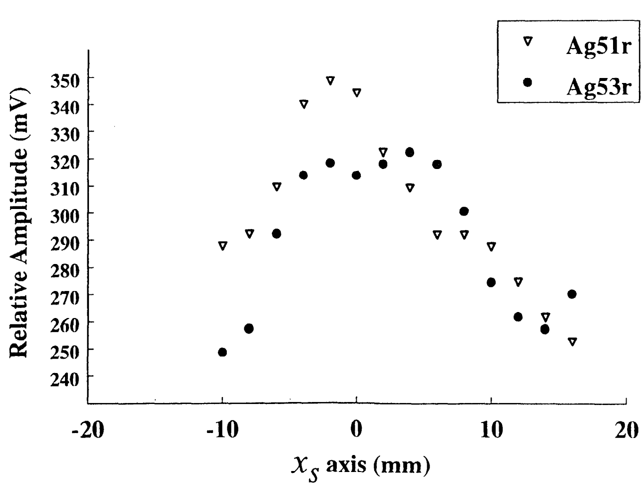

Figure 9. Averaged relative amplitude of acoustic events perpendicular to fault (x_S axis) for two cores with identical piezoceramic trigger setup but different total lengths of the frozen-in shear rupture.

the fault plane (≈ 20°) than on the dilational side (≈ 70°). However, average fault plane solutions of S-type AE events show no difference in their overall orientation on both sides of the fault (Figure 10). Since we used cumulative AE events irrespective of the hypocenter distance from the fracture, it is possible that different orientations do not show up. A second explanation is that our experimentally induced fracture is not pure mode 2; for example, mode 3 faulting would result in a symmetrical orientation distribution of process zone cracks on either side of the fault at 45°.

In Figure 12 the acoustic width of the process zone is shown versus confining pressure. Two preliminary results at 10 and 40 MPa suggest that the width of the zone approaches a constant value at higher pressures (~10 average grain diameter). At low confining pressure (p< 10 MPa) a bifurcation of the curve is evident which comes from the speed of fault. At zero pressure, slow faults produce a narrow (9 mm) while fast faults produce a broader (17 mm) process zone.

4.2. Scaling Relationships

The length of the process zone S (also called the length of the frictional breakdown zone [*Cowie and Scholz*, 1992b]) is estimated from acoustic data of sample Ag51r for which the rupture stopped inside the sensor array (Figure 6a). S is ≈ 19 mm, which corresponds to ~15 times the average grain size (Figure 11, S_{AE}). The ratio S/L = 0.17 for core Ag51r is in good agreement with the result of S/L=0.18 of *Cowie and Scholz* [1992b]. From the study of *Moore and Lockner* [1995, Figures 1 and 5a] a smaller ratio of S/L ≈ 0.12 is inferred. For the same core the length of process zone is about twice the width of the process zone (S_{AE}/w_{AE}=2). *Cowie and Scholz* [1992b] and *Scholz et al.* [1993] suggested that the length of the process zone and its width increase as the fault propagates away from the nucleation site. The AE-based FPZ width varies, but there is no trend indicating a systematic increase of width with fracture length (Figure 6). This may be due to our loading conditions.

Process zone properties and calculated fault scaling relationships are summarized in Table 3. In addition to the AE rate-controlled tests (Tables 1 and 2), we also included data from displacement-controlled tests on similar Aue granite samples [*Zang et al.*, 1998]. The width of the acoustic process zone (Table 3, w_{AE}) is generally larger for displacement-controlled than for AE rate-controlled tests. The propagation velocity of the process zone tip in these two types of experiments differed drastically; it ranged between ≈ 2 mm/s in displacement-controlled experiments to 2 μm/s for sample Ag53r in an AE rate-controlled run. The "acoustic" FPZ, as

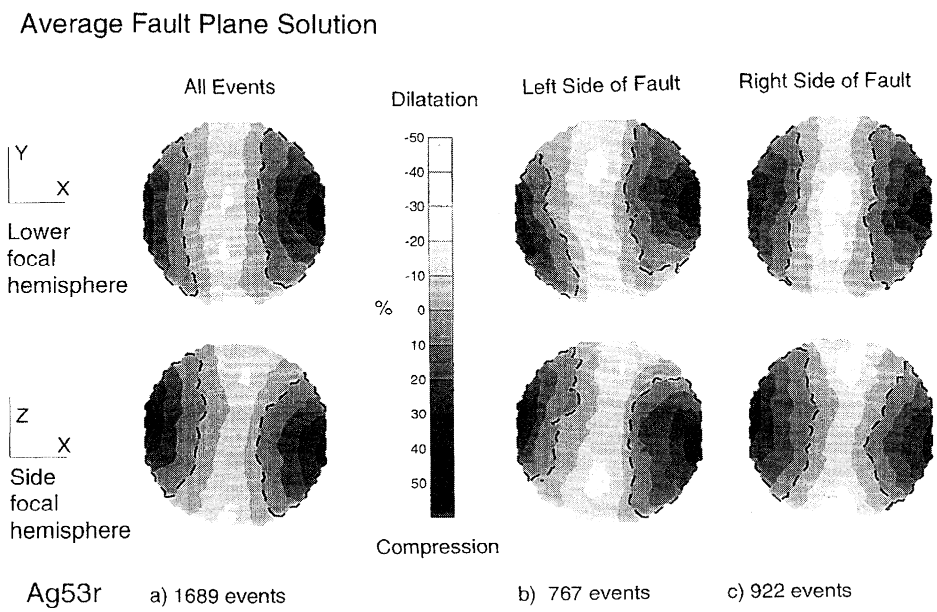

Figure 10. Average fault plane solutions for (a) the total number of located S-type acoustic events in core Ag53r, (b) events generated only from the dilatational side of fault, and (c) events generated only from the compressive side of fault.

observed in sample Ag53r, is about half as wide as for a $\approx 10^3$ times faster propagating fracture (Ag1r). This suggests that faster fractures may produce larger process zones and not only depend on material properties [*Zietlow and Labuz,* 1998] or fault length [*Scholz et al.* 1993].

Fault scaling relationships postulated by *Scholz et al.* [1993] are summarized in Table 3 and compared to the results of this study (Table 3, d, L, w_{AE}, and w_c). The ratios of process zone width to total fault length $w_{AE}/2L$ and $w_c/2L$ fall within the predicted range of 0.01-0.1; the crack data result in values $\approx$ 0.01, and the acoustic emission data give values $\approx$ 0.1. Our average laboratory value $w_c/2L = 0.018$ is in good agreement with the slope value 0.016 recently published by *Vermilye and Scholz* [1998]. Their data are from natural faults that cover >7 orders of magnitude in length. *Cowie and Scholz* [1992b] and *Scholz et al.* [1993] argue that d is linearly related to L with a ratio $d/2L$ in the range of $\approx 10^{-2}$-10^{-3}. Our data indicate a ratio $d/2L \approx 10^{-3}$.

4.3. Shear Fracture Energy

The strain rate released during the formation of a fracture is dissipated as heat, elastic waves, plastic deformation, and crack surface area [*Olgaard and Brace,* 1983]. The average crack density of process zone-related cracks in sample Ag53r is 1 mm/mm^2. With the cumulative volume of the acoustic process zone w_{AE} (90 mm (length) x 40 mm (width) x 9 mm) the total surface area of process zone microcracks is 324×10^{-4} m^2. The total area of the macrofracture is 36×10^{-4} m^2. Multiplied by a typical value of specific fracture surface energy of granite (e.g., 56 J m^{-2} [Scholz, 1990, p. 24]), we have a total crack surface energy of 2.0 J for sample Ag53r. This corresponds to ~29% of the total work expended during deformation of the sample until the fracture formed.

Using data from the wide-band sensor attached to the samples, we can roughly estimate the energy dissipated in

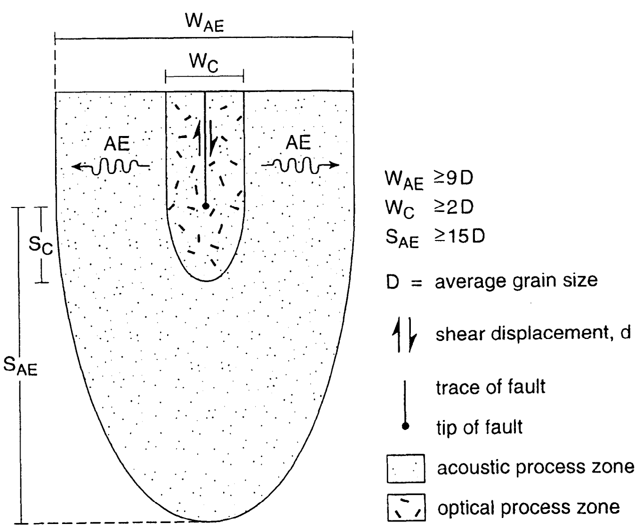

Figure 11. Synoptic picture of the process zone in Aue granite as determined by acoustic emission and thin section analysis.

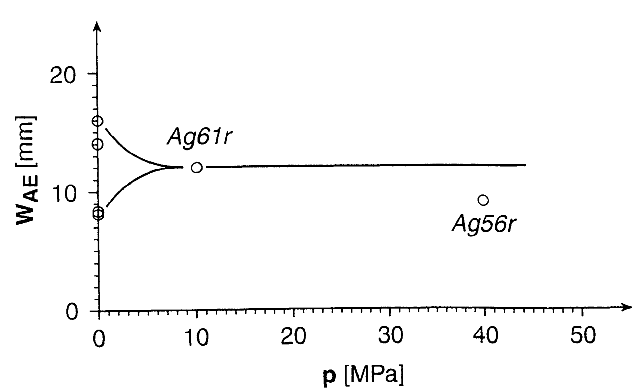

Figure 12. Acoustic width of the fracture process zone versus confining pressure. Different values at zero pressure denote experiments with different speed of faults.

acoustic emissions. Calibration of the sensor gave an approximate energy of 33 μJ for a 1 mV s signal in red granite. After the propagating process zone reached the bottom of the sample, the accumulated AE energy was ~0.1 J, i.e., ~1.5% of the total work done on the sample.

Acknowledgments. We are grateful to the Associate Editor Harry Green (Riverside, California) and the reviewer, David Lockner (Menlo Park, California) for constructive comments on an earlier version of the paper.

References

Barenblatt, G. I., The mathematical theory of equilibrium cracks in brittle fracture, *Adv. Appl. Mech.*, *7*, 55-129, 1962.

Barton, C. C., Variables in fracture energy and toughness testing of rock, paper presented at 23rd U.S. Symposium on Rock Mechanics, Association Engineering Geologists, Berkeley, Calif., 1982.

Chester, F. M., and J. M. Logan, Implications for mechanical properties of brittle faults from observations of the Punchbowl fault zone, California, *Pure Appl. Geophys.*, *124*, 79-106, 1986.

Cowie, P. A., and C. H. Scholz, Growth of faults by accumulation of seismic slip, *J. Geophys. Res.*, *97*(B7), 11,085-11,095, 1992a.

Cowie, P. A., and C. H. Scholz, Physical explanation for the displacement-length relationship of faults using a post-yield fracture mechanics model, *J. Struct. Geol.*, *14*(10), 1133-1148, 1992b.

Cox, B. N., and D. B. Marshall, Overview 111: Concepts for bridged cracks in fracture and fatigue. *Acta Metall. Mater.*, *42*, 341-363, 1994.

Dugdale, D. S., Yielding of steel sheets containing slits, *J. Mech. Phys. Solids*, *8*, 100-104, 1960.

Dyskin, A. V., Crack growth criteria incorporating non-singular stresses: Size effect in apparent fracture toughness, *Int. J. Fract.*, *83*, 191-206, 1997.

Ellsworth, W. L., and G. C. Beroza, Seismic evidence for an earthquake nucleation phase, *Science*, *268*, 851-855, 1995.

Evans, A. G., A. H. Heuer, and D. L. Potter, The fracture toughness of ceramics, in *Fracture*, vol. I, ICF4, pp. 529-556, Waterloo, Ontario, Canada, 1977.

Friedman, M., J. Handin, and G. Alani, Fracture-surface energy of rocks, *Int. J. Rock Mech. Min. Sci.*, *9*, 757-766, 1972.

Goodier, J. N., Mathematical theory of equilibrium cracks, In *Fracture, An Advanced Treatise*, vol. 2, *Mathematical Fundamentals*, edited by H. Liebowitz, pp. 1-66, Academic, San Diego, Calif., 1968.

Granryd, L., I. C. Getting, and H. Spetzler, Path dependence of acoustic velocity and attenuation in experimentally deformed westerly granite, *Geophys. Res. Lett.*, *10*, 71-74, 1983.

Hoagland, R. G., and J. D. Embury, A treatment of inelastic deformation around a crack tip due to microcracking, *J. Am. Ceram. Society*, *63*, 404-410, 1979.

Hoagland, R. G., G. T. Hahn, and A. R. Rosenfield, Influence of microstructure on fracture propagation in rock, *Rock Mech.*, *5*, 77-106, 1973.

Hoshide, T., Grain fracture model and its application to strength evaluation in engineering ceramics, *Eng. Frac. Mech.*, *44*, 403-408, 1993.

Hutchinson, J. W., Crack tip shielding by micro-cracking in brittle solids, *Acta Metall. Mater.*, *35*, 1605-1619, 1987.

Janssen, C., F. C. Wagner, A. Zang, and G. Dresen, Fracture process zone in granite A microstructural analysis. *Int. J. Earth Sciences*, in press, 2000.

Labuz, J. F., and L. Biolzi, Characteristic strength of quasi-brittle materials, *Int. J. Solids Struct.*, *35* (31-32), 4191-4203, 1998.

Labuz, J. F., S. P. Shah, and C. H. Dowding, Post peak tensile load-displacement response and the fracture process zone in rock, paper presented at 24rd U.S. Symposium on Rock Mechanics, Association Engineering Geologists, College Station, Tex., 1983.

Labuz, J. F., S. P. Shah, and C. H. Dowding, The fracture process zone in granite: Evidence and effect, *Int. J. Rock Mech. Geomech. Abstr.*, *24* (4), 235-246, 1987.

Lei, X., K. Kusunose, M. V. M. S. Rao, O. Nishizawa, and T. Satoh, Quasi-static fault growth and cracking inhomogeneous brittle rock under triaxial compression using acoustic emission monitoring, *J. Geophys. Res.*, *105*(B3), 6127-6139, 2000.

Lockner, D. A., The role of acoustic emission in the study of rock, *Int. J. Rock Mech. Min. Sci. Geomech. Abstr.*, *30*(7), 883-899, 1993.

Lockner, D. A., Brittle fracture as an analog to earthquakes: Can acoustic emission be used to develop a viable prediction strategy?, *J. Acoust. Emission*, *14*(3-4), 1996.

Lockner, D.A., J. D. Byerlee, V. Kuksenko, A. Ponomarev, and A. Sidorin, Quasi-static fault growth and shear fracture energy in granite, *Nature*, *350*, 39-42, 1991.

Lockner, D. A., D. E. Moore, and Z. Reches, Microcrack interaction leading to shear fracture, in *Rock Mechanics*, edited by J. R. Tillerson and W. R. Wawersik, pp. 807-816, A. A. Balkema, Brookfield, Ut., 1992.

Madden, T. R., Microcrack connectivity in rocks: A renormalisation group approach to the critical phenomena of conduction and failure in crystallin rocks, *J. Geophys. Res.*, *88*(B1), 585-592, 1983.

Moore, D. E., and D. A. Lockner, The role of microcracking in shear-fracture propagation in granite, *J. Struct. Geol.*, *17*(1), 95-114, 1995.

Nemat-Nasser, S., and M. Horii, Toughening by partial or full bridging of cracks in ceramics and fibre reinforced composites, *Mech. Mater.*, *6*, 245-269, 1987.

Neuber, H., *Kerbspannungslehre*, 1, *Auflage*, Springer-Verlag, New York, 1937.

Olgaard, D. L., and W. F. Brace, The microstructure of gouge from mining-induced seismic shear zone, *Int. J. Rock. Mech. Min. Sci. Geomech. Abstr.*, *20*, 11-19, 1983.

Ouchterlony, F., Review of fracture toughness testing of rocks, *DS 1980 15*, Swed. Detonic Res. Found., Stockholm, 1980.

Press, W. H., B. P. Flamery, S. Tenkolsky, and W. T. Vetterling, *Numerical Recipes*, 702 pp., Cambridge Univ. Press, New York, 1987.

Reches, Z., and D. A. Lockner, Nucleation and growth of faults in brittle rocks, *J. Geophys. Res.*, *99*(B9), 18,159-18,173, 1994.

Rice, J. R., The mechanics of earthquake rupture, *Physics of Earth's Interior*, edited by A. Dziewonski and E. Boschi, pp. 555-649, North-Holland, New York ,1980.

Rossmanith, H. P., Modelling of fracture process zones and singularity dominated zones, *Eng. Fract. Mech.*, 17, 509-525, 1983.

Scholz, C. H., N. H. Dawers, J.-Z. Yu, M. H. Anders, and P. A. Cowie, Fault growth and scaling laws: Preliminary results, *J. Geophys. Res.*, *98*(B12), 21,951-21,961, 1993.

Shum, D. K. M., Analysis of stable crack growth in brittle materials, part I, A process zone model, *Int. J. Fract.*, *75*, 95-114, 1996.

Swanson, P. L., Tensile fracture resistance mechanisms in brittle polycrystals: An ultrasonics and in situ microscopy investigation, *J. Geophys. Res*, *92*(B8), 8015-8036, 1987.

Vermilye, J. M., The growth of natural fracture systems: A fracture mechanics approach, Ph.D. thesis, 236 pp., Columbia Univ., New York, 1996.

Vermilye, J. M., and C. H. Scholz, The process zone: A microstructural view of fault growth, *J. Geophys. Res.*, *103*(B6), 12,223-12,237, 1998.

Wieghardt, K., Über das Spalten und Zerreiben elastischer Körper, *Ztg. Math. Phys.*, *55*, 60-103, 1907.

Wong, T. F., Micromechanics of faulting in Westerly granite, *Int. J. Rock. Mech. Min. Sci. Geomech. Abstr.*, *19*, 49-64, 1982.

Zang, A., F. C. Wagner, S. Stanchits, G. Dresen, R. Andresen, and M. A. Haidekker, Source analysis of acoustic emissions in Aue granite cores under symmetric and asymmetric compressive loads, *Geophys. J. Int.*, *135*, 1113-1130, 1998.

Zietlow, W. K. and J. F. Labuz, Measurement of the intrinsic process zone in rock using acoustic emission, *Int. J. Rock Mech. Min. Sci. Geomech. Abstr.*, *35*, 291-299, 1998.

G. Dresen, C. Janssen, F. C. Wagner and A. Zang, GeoForschungs-Zentrum, Telegrafenberg, 14473 Potsdam, Germany. (dre@gfz-potsdam.de)

S. Stanchits, U. S. Geological Survey, 345 Middlefield Road, MS/977, Menlo Park, CA 94025. (sstanchits@isdmnl.wr.usgs.gov)

(Received September 30, 1999; revised June 16, 2000; accepted June 28, 2000.)